Three-dimensional structure and formation mechanisms of Y2O3 hollow-precipitates in a Cu-based metallic glass

Oriane Baulin, Thierry Douillard, Damien Fabrègue, Michel Perez, Jean-Marc Pelletier, Matthieu Bugnet

Three-dimensional structure and formation mechanisms of Y_2O_3 hollow-precipitates in a Cu-based metallic glass

Oriane Baulin*, Thierry Douillard, Damien Fabregue, Michel Perez, Jean-Marc Pelletier, Matthieu Bugnet*

Univ Lyon, INSA-Lyon, Univ Claude Bernard Lyon 1, MATEIS, UMR CNRS 5510, 20 avenue Albert Einstein, F-69621 Villeurbanne, France

Corresponding author: oriane.baulin@insa-lyon.fr ; matthieu.bugnet@insa-lyon.fr

Abstract

Recently, the high ductility of Cu-based bulk metallic glasses (BMGs) has been directly linked to the presence of Y_2O_3 precipitates, and surrounding crystallized areas. Nevertheless, the formation of the precipitates remains to be defined. In this work, the structure of Y_2O_3 precipitates and crystallized zones of the BMG are investigated at the nanoscale in three-dimensions, shining light on their spatial distribution and their origin. Two kinds of precipitates were observed: small solid ones and large hollow ones. The mechanism proposed to explain the formation of hollow-precipitates is based on the Kirkendall effect. A model was implemented to assess the feasibility of this mechanism with the experimental results. Moreover, our results suggest that micro and nano-crystallized areas within the BMG are induced by the presence of yttria precipitates, with a correspondence between the size of the precipitate and the size of the crystallized areas.

Keywords: Bulk Metallic Glasses, Microscopy, Kirkendall effect, Yttrium, Y_2O_3 precipitates

1 Introduction

Bulk metallic glasses (BMGs) are materials attracting broad interest from the materials community with a wide range of industrial applications in fields as diverse as sports, watchmaking, biomedical, and electronics. [1-4]. Due to the absence of long-distance order, grain boundaries and other structural defects such as dislocations, BMGs exhibit promising properties: high yield strength [5, 6] (about 2 GPa for Cu-based BMGs [7]), and high corrosion resistance [8, 9] among others. However, they also often exhibit two main drawbacks. Firstly, they reveal a restricted thin section due to the necessary high cooling rate. Secondly, they also show a catastrophic failure in tension and a

quasi-brittle fracture under compressive solicitations with limited ductility [10-12]. To increase the ductility in BMGs, a large number of possibilities are available. Firstly, *in situ* processing can be achieved through proper thermal treatment to promote the crystallization of some phases [13] such as the β dendrite reinforced Ti-based BMGCs [14], or via the addition of very high melting point particles, like Ta [15] or U [16]. Composites can also be produced *ex situ* using powder metallurgy and the addition of crystalline particles [17-21]. For example, the ductility increase of a novel kind of Zr-based metallic glass reinforced with tungsten springs were studied recently [22]. A second way to increase the ductility is the introduction of defects by mechanical processes (rejuvenation, severe plastic deformation…) [23-25], or minor additions of a wide variety of elements (metallic, metalloid or rare-earth elements) [26-28].

Minor additions of proper elements can induce a drastic increase on the glass forming ability and significant improvement of the mechanical properties [29-32]. Rare-earth elements (REE) are a very attractive category of components for this purpose. In particular, their stability, their large atomic ratio, and their ability to stabilize the liquid phase and to decrease the liquidus temperature close to a eutectic composition, are of interest [27]. In the past decades, the addition of yttrium has been studied for its strong affinity with oxygen, and its ability to form innocuous yttrium oxides, especially in the Cu-based systems [33-39]. It has already been highlighted in a previous work that only a small amount of yttrium (about 1 at. % is the optimum) in Cu-Zr-Ti system is beneficial to increase the ductility by 2 points [33]. This enhancement of mechanical properties has been suggested to arise from Y_2O_3 crystalline precipitates, surrounded by nano- and micro-crystallized areas formation in the BMG, depending on the size of the precipitates. However, the formation mechanism of these precipitates remains unclear.

In this work, the structure and chemistry of two kinds of precipitates, full and hollow, were investigated. Further information about their spatial distribution in the sample, and their role on the formation of crystallized areas were obtained from three-dimensional reconstructions using the focused ion beam (FIB) technique. This original approach could foster the understanding of precipitation in metallic glasses, and consequently paves the way toward designing new metallic

glasses with specific properties, through precise control of the nature and volume fraction of the precipitates and crystallized areas. Engineered structural materials such as metallic glasses containing precipitates are particularly relevant to increase the ductility of these materials, which is their main drawback. Ultimately, this approach might lead to the creation of ductile composites with an amorphous matrix.

The formation of the precipitates was explained on the basis of diffusion mechanisms and the Kirkendall effect (KE), which was first highlighted observing Cu-Zn diffusion couple [40]. Nowadays, the KE is purposely used to obtain hollow nanostructures in a wide range of materials [41-43]. Modelling this effect has been a topic of great interest, studied by Desgranges and Nastar [44]. In this work, a model based on the KE is proposed and discussed to explain the formation of the largest hollow precipitates.

2 Experimental Procedure

2.1 Sample Preparation

Master ingots of the composition $(Cu_{60}Zr_{30}Ti_{10})_{99}Y_1$ were prepared using pure materials Cu (99.9%), Zr(99.9%), Ti (99.9%) and Y (99.9%). This composition has been found to show the highest ductility in a previous work [33]. The ingots were melted six times to obtain a good chemical homogeneity by arc melting under Ar and Zr-gettered atmosphere. The 3-mm rods samples were processed with suction casting in a copper mould. The composition was also checked by using an energy-dispersive X-ray system (EDXS) with an X-max 80 mm² Silicon Drift Detector (Oxford Instruments, Abingdon, Oxfordshire, UK) in combination with a SEM (Supra 55VP, Carl Zeiss Microscopy GmbH, Jena, Germany), at 10 kV for the acceleration voltage.

2.2 TEM Experiments

To investigate the sample microstructure using transmission electron microscopy (TEM), a 0.5 mm thick slice was cut with a micro-chainsaw. The thickness was then mechanically reduced using a GATAN dimpler grinder device. Finally, an ion polishing system (GATAN 691 PIPS) was used to finish the sample preparation, with milling angles equal to -10° and +10°, at 4 kV during 4 hours.

TEM has been conducted with an ETEM Titan G2 80-300, corrected for spherical aberration in TEM mode, and equipped with a STEM-HAADF imaging module, an EDX spectrometer (Xmax 80mm², Oxford NanoAnalysis Instruments, Abingdon, Oxfordshire, UK), an electron energy-loss spectrometer Gatan imaging filter Tridiem ERS, and a 16 Mega-pixels high speed and optimized-CMOS sensitivity Oneview camera (Gatan Inc., Pleasanton, USA).

2.3 Scanning electron microscopy (SEM), Backscattered electron (BSE), Scanning ion microscopy (SIM) experiments

The largest crystallized areas have been identified and analyzed by scanning electron microscopy (SEM) and scanning ion microscopy (SIM). The image formation in a SEM is dependent on signals produced from the interaction of the electron beam with the sample. Among them, secondary electrons (SE) and backscattered electrons (BSE) are used to form images. Operating in SE mode in low voltage SEM on a flat surface can give rise to contrasts whose interpretation is often difficult. However, these contrasts can provide relevant structural or physical information (Schottky barrier contrast, voltage contrast, charging contrast …). Also, the contrasts obtained under these conditions may become material and crystallographic dependent [45]. Moreover, an advantage to low-beam-energy operation is the increase in the yield of SE produced, allowing an improved signal-to noise performance [46]. BSE are primary beam electrons interacting with the atomic nucleus, and escaping from the sample with a distributed energy-loss (when incidence is normal). The emission volume of the BSE depends on the mean atomic number of the sample and of the accelerating voltage of the primary beam electrons. Both SE and BSE imaging were performed at an accelerating voltage of 1.5 keV and using an in-column detection. Besides, in front of the entry system of the BSE detector, an energy filtering grid was set to 800 V to improve the spatial resolution.

The contrast of SIM images is similar to SEM, with a higher sensitivity to surface topography, even if the ion implantation induces more damages on the sample surface. Indeed, ion-matter interactions also create secondary ions, whose intensity mainly depends on the atomic number of excited atoms (ISI for ion induced secondary ions). Thus, collected by a secondary ion (SI) detector, the ISI signal highlights the chemical contrast of the microstructure. ISI emission yield is not yet fully

understood. However, it seems that the presence of oxygen can greatly enhance the ISI yield [47, 48]. SIM imaging was achieved within the FIB apparatus, at 30 keV and 80pA.

2.4 Focused ion beam (FIB) method

A FIB/SEM workstation (NVision 40, Carl Zeiss Microscopy GmbH, Oberkochen, Germany), combining a SIINT zeta FIB column (Seiko Instruments Inc. NanoTechnology, Japan) with a Gemini I column, has been employed to analyse the structure of the yttria precipitates, and build a 3D distribution of these latter and the surrounding volumes, using a voxel size of $5\times5\times5$ nm^3. To conduct this experiment, the protocol described in Fig. 1 has been followed. First, a carbon layer was deposited on the volume of interest induced by *in situ* ion beam. The purpose is to smooth out the surface roughness during slicing in order to achieve sharp upper edges and minimize curtaining artefacts. Then, several reference lines were imprinted into the carbon layer and filled *in situ* with tungsten for reliable post-stack alignment purposes (Fig. 1). Prior to serial sectioning, a slice was milled to a depth that freed up a sufficient cross-sectional surface. This step was performed with a coarse ion beam current of 27 nA with an accelerating voltage of 30 keV. Then, serial FIB sectioning was done with a current of 700 pA at 30 keV. SEM imaging was done in secondary electrons (SE) mode with an accelerating voltage of 1.5 keV simultaneously with a classic Everhart-Thornley detector and an In-lens detector. The acquisition has been performed with NanoPatterning and Visualisation Engine (NPVE) – FIBICS. All the image processing and analyses was performed with Fiji, an open source image processing package based on ImageJ software [49]. Registration was achieved on the reference lines, and segmentation was then done for each slice using contrast thresholding, thus allowing for subsequent 3D viewing. After data cropping, a volume of $4.9\times4.75\times4.1$ µm^3 was obtained.

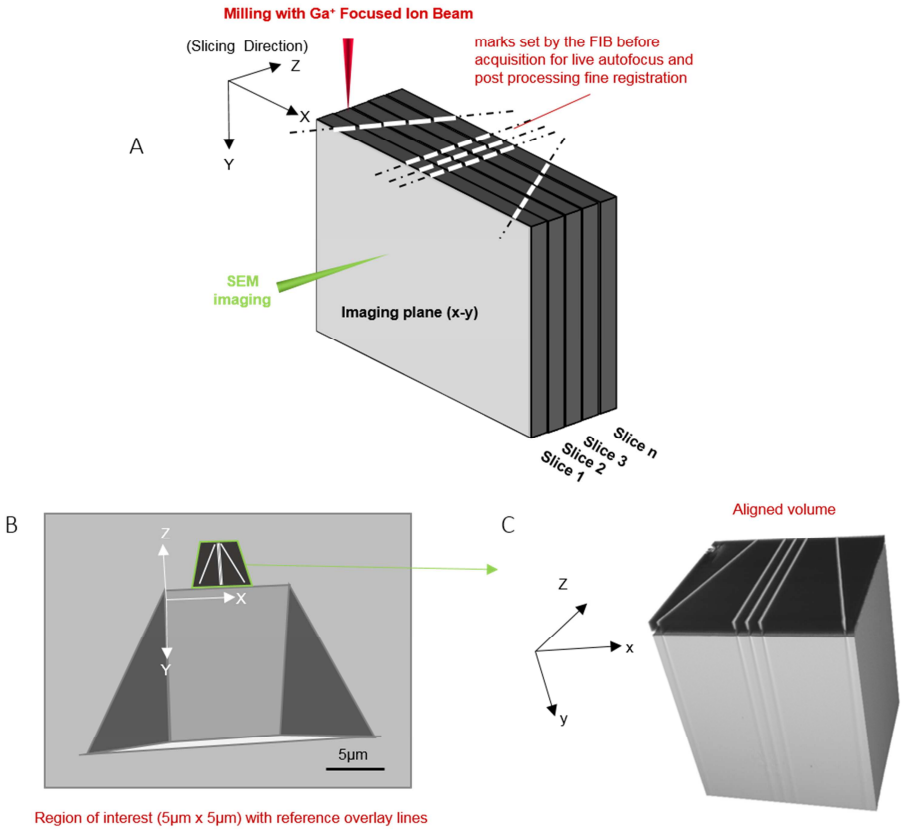

Figure 1: Schematic representation of the processing of tomography improved with a refined drift correction procedure. (A) Schematic illustration showing the pattern of reference marks used for the post-acquisition slice registration (B) Schematic illustration of the reference chevron pattern overlaid to the region of interest. These reference notches consist of imprinted electron beam induced tungsten deposition into an ion beam induced carbon coating (C) Example of an extracted registered volume.

3 Results

3.1. Chemical analysis of the Y_2O_3 precipitates and the surrounding crystalline phases.

To understand the origins and the mechanisms behind the ductility improvement of this bulk metallic glass with an optimum of 1 at. % Y [33], accurate analysis with TEM experiments were conducted to determine the chemical nature and the structure of the precipitate and their surroundings. The chemical nature of the precipitate has already been determined by electron energy-loss spectroscopy (EELS) and EDX measurements [33]. The bright field TEM images in Fig. 2a) and Fig.

2b) highlight the existence of two types of precipitates: large (~200 nm long) rectangular precipitates, containing a cavity (~60 nm long) in the middle, and smaller precipitates (~50 to 100 nm long) without any cavity. The largest precipitates are surrounded by significant micro-crystallized areas (Fig. 2a)). It is worth noting that the crystallized area seemed to be composed of two different phases: a Cu-rich phase, in addition to a Ti-rich phase according to the EDX maps in Fig. 2c). The Cu-rich areas correspond to Ti-poor areas, and vice-versa. According to these results, a size threshold seems to control the presence or absence of the cavity, and the crystallized area development.

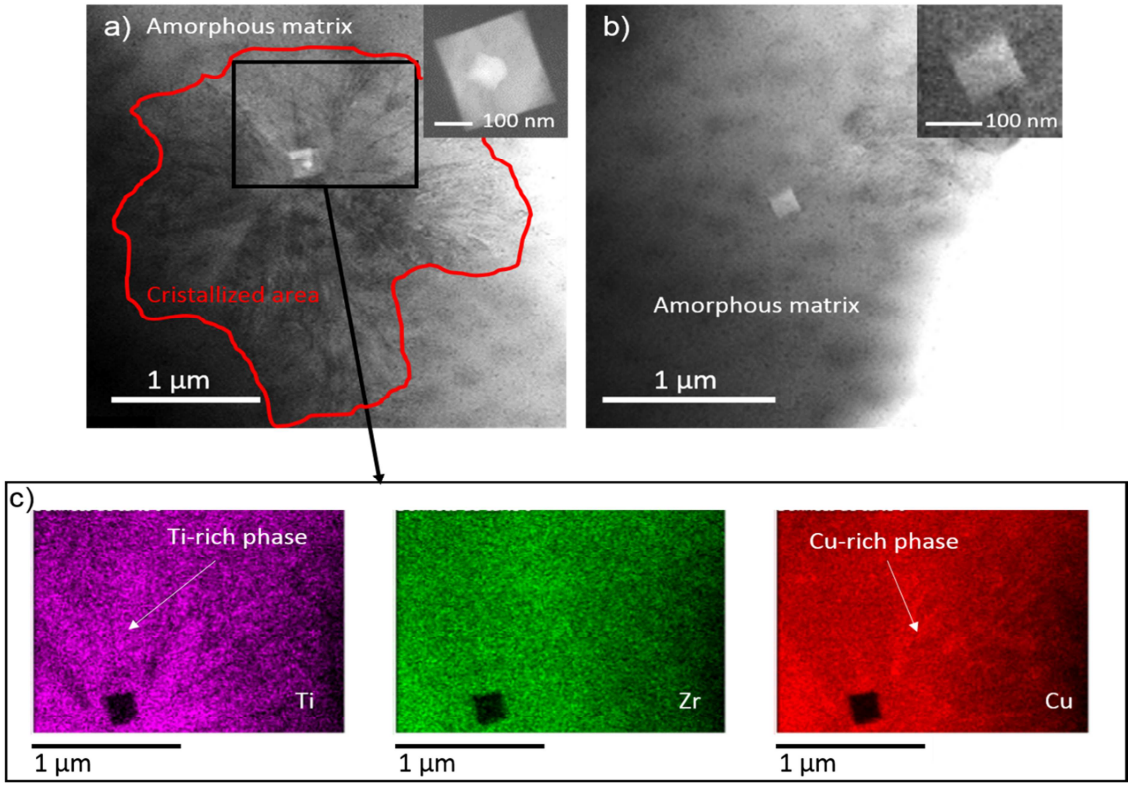

Figure 2: a) Bright field TEM image of a large precipitate with micro-crystallised area, b) bright field TEM image of the small precipitate, c) chemical analysis of the precipitates and surroundings

The presence of precipitates and crystallized areas plays an extremely significant role in the mechanical properties [33]. The rationale behind this structure-property relationship requires quantifying the distribution of precipitates and crystallized zones, and understanding their formation, which is the topic of the next section.

3.2 SEM and SIM observations

SEM and SIM observations shown in Fig. 3 provide information about the spatial distribution on the sample surface, the structural relationship between the precipitates and the crystalline areas, and their surface density. The crystallite size is evaluated between 1 and 3 µm. Their surface density has been measured to be about 5%. This fraction is significant for an X-ray amorphous sample, and is expected to be representative of the material, as SEM observations have been conducted on large areas. Fig. 3a) is a low magnification SEM image, which highlights the homogeneous distribution of the crystallized areas in the sample. Furthermore, another interesting result can be inferred from the higher magnification images in Fig. 3b-d): in all visible precipitates associated with crystallized areas, the yttria precipitate is clearly localized in the middle of the dendrites.

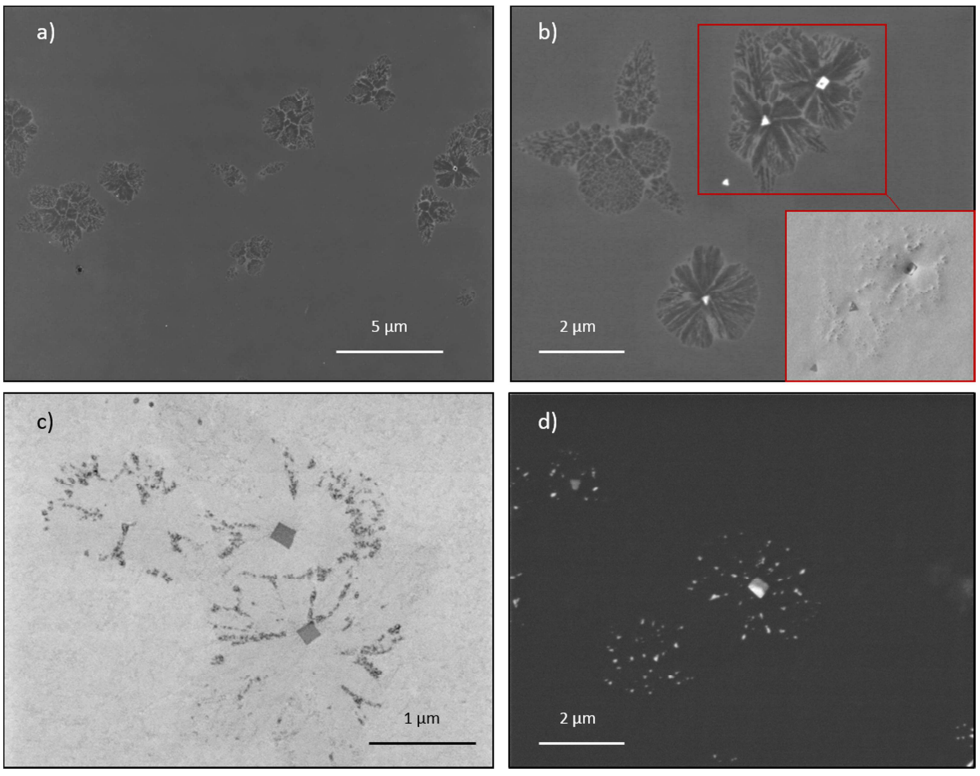

Figure 3: SEM and SIM surface characterization of a polished BMG. (a) Representative visualization of the distribution of the crystalline areas (In-Lens low voltage SE imaging). (b) Visualization of a few crystalline areas with a few yttria precipitates (bright contrast in In-Lens low voltage SE imaging). A random cross-section of these cubic precipitates leads to a triangular shape in 2D. Insert is a standard Everhart-Thornley SE imaging of a selected area which shows more punctual elements (small dark contrasts) within the dendrite. (c) Low Loss in-lens BSE imaging of a dendritic like area. yttria precipitates are dark. Small dark contrasts are visible within the

crystalline areas (d) ISI-SIM imaging. yttria precipitates are whites. Other more punctual areas light up around these precipitates

3.3 3D distribution of the precipitates and crystallized phases in the volume

Focused ion beam has been used to study the distribution of the crystalline phases in a small volume ($4.9 \times 4.75 \times 4.1$ μm^3) of the sample (Fig. 4a)). According to the results of the FIB experiment and reconstruction shown in Fig. 4b), only one 200 nm long precipitate with an internal cavity is visible in this volume, inducing a significant crystallized area. However, a large number of smaller precipitates are homogeneously distributed in the volume. The proportion of precipitates (yellow particles in Fig. 4) and crystallized areas is evaluated to ~0.1 % and ~7.7 %, respectively. Fig. 4c) shows that yttria precipitates are located at the centre of all crystallized areas (yellow and red colours in Fig. 4), and could be the precursors of the matrix crystallization. Fig. 4a) and b) highlight a correlation between the size of the precipitates and the one of the induced crystallized areas. Indeed, two kinds of crystalline areas are present: the micro-areas (~1-2 µm) form around a large hollow precipitate (~ 200 nm long), and the nano-areas (~100 nm) induced by the small solid precipitates about 50-100 nm long. Only few crystallized areas can be observed in the volume without the presence of a precipitate at its core. Small full precipitates are not always associated with crystallized areas, as some of them remain isolated in the amorphous matrix (see Fig. 4c)). Fig. 4d) shows a reconstructed view of an area of the sample. Some small yttria precipitates are also within the most significant crystallized area, however not in the middle.

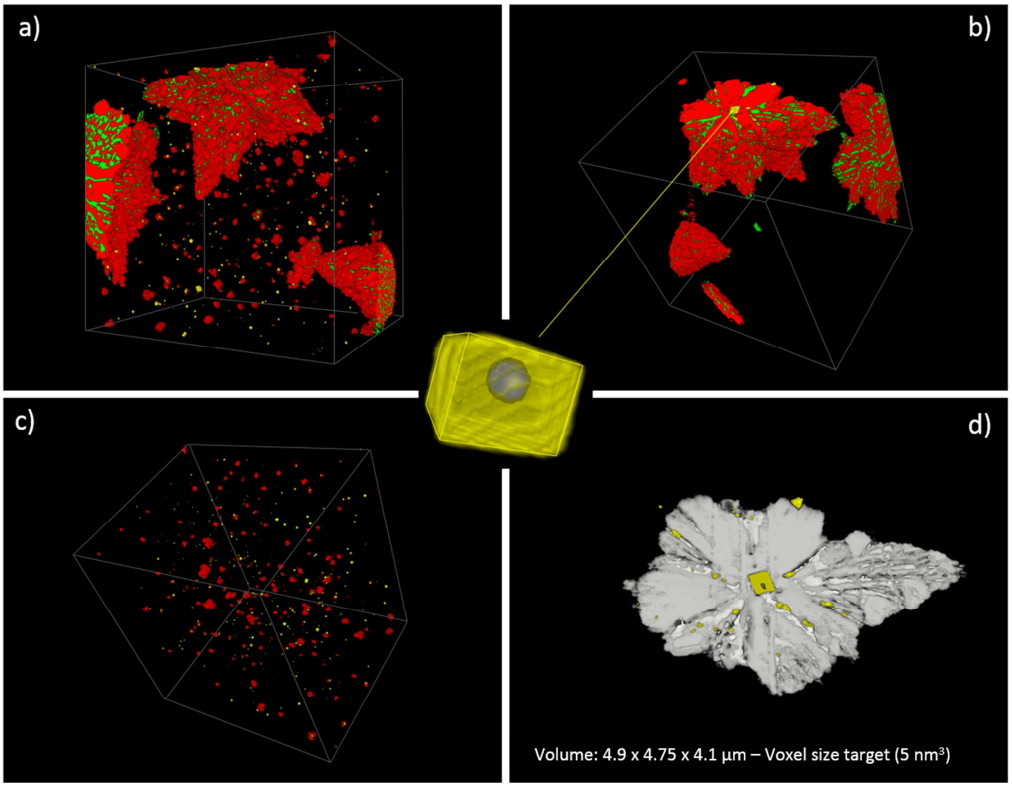

Figure 4: 3D FIB/SEM reconstructed views of (a) all assumed crystalline phases within the volume: cuboid yttria in yellow, monophase (red) or polyphase (red and green colour mixing) dendrite-like structures. (b) extracted from the volume, only dendrite-like structures detected in 2D by surface observations in SEM (7.6% vol here). Tree-like branched crystal structure with at least 2 phases (red and green) – in this volume, within such a significant crystallized area, a cuboid precipitate (220 nm x 140 nm x 215 nm) in yellow contain a nanometeric pore. (c) extracted from the volume, only nano-crystalline volumes which have not been detected in SEM - in red: small monophase crystalline phases (0.08% vol, diameter around 100 nm) and cuboid precipitate (0.01% vol, width less than or equal to 50 nm). These 2 phases are sometimes closely linked or separated: 40% of yellow cuboid inside red small diffuse crystalline area. *a priori*, 25% of standalone red small diffuse crystalline. (d) reconstructed view of an area similar to those seen in Fig 1 (in iSI imaging especially). Some small yttria precipitates are also within the most significant crystallized areas.

4 Discussion

4.1 Role of the precipitates on the crystallized areas formation

The results seem to suggest that the crystallized areas are induced by the presence of the precipitates. From these observations, a scenario can be suggested: the precipitates act as heterogeneous nucleation sites for the crystalline areas. As the size of these areas seems to be related to the size of the precipitates, the latter seem to play a significant role on the formation and development of the crystallized zones.

As the cooling is too fast to form the precipitates, the precipitation most probably takes place in the liquid phase, during the melting. Considering the strong affinity between yttrium and oxygen, and the free energy of formation (ΔH_f =-1932 kJ/mol, compared to -950 kJ/mol and -1097 kJ/mol for TiO_2 and ZrO_2, respectively), the precipitates should form very quickly during the melting.

The small precipitates stand in the middle of smaller crystallized areas. This is a type of particle simulated nucleation. It should be due first to a gain in terms of surface energy for the nucleation, and also to a possible local change in the glass chemical composition in the surroundings of the precipitates.

The presence of crystallized areas in the amorphous matrix induces the formation of an *in situ* composite sample, extended by crystalline zones. This could explain the observed ductility enhancement reported previously [33]. Shear band movement is responsible for the deformation and the plasticity in metallic glasses [50, 51]. Crystalline areas act as nucleation sites for shear bands and allow the simultaneous initiation of multiple bands. Moreover, these zones hinder the shear band displacement, which also leads to a better ductility. However, these areas could be too large or too numerous if the yttrium amount exceeds an optimum, which leads to a decrease of the ductility [33]. Nevertheless, the influence of the size of the crystalline areas on this mechanism remains unclear.

4.3 Explanation on the cavity formation in the Y_2O_3 precipitates

The formation of the cavity is assumed to be based on the Kirkendall effect (KE). This effect comes from the difference of diffusion rates between two species, namely yttrium and oxygen, which can be present as impurities in the raw materials Zr or Ti. Based on previous works on hollow oxides formed by KE, metal atoms diffuse faster than oxygen in the oxide layer [52]. The unbalanced atomic fluxes are balanced by a vacancy flux: $J_V = J_Y - J_O$. In the present case, a Y-rich area is considered initially. Oxygen diffuses inwards with a vacancy flux, as yttrium diffuses outwards, as shown in Fig. 5. An oxide layer is formed as a result of the strong affinity between oxygen and yttrium, which react immediately to form Y_2O_3. This phenomenon leads to the formation of a void, within the Y-rich

particles, where all vacancies cluster. For the smaller precipitates, the vacancies are ejected outside due to a higher surface/volume ratio. A size threshold seems to be linked to the presence of a cavity in the middle of the yttria precipitate: the cavity appears if the precipitate is large enough.

To confirm this scenario with the elaboration process parameters, a simple diffusion model was implemented. Some hypotheses were used to simplify the model. Firstly, a spherical geometry was considered. Secondly, a stationary diffusion state was considered. The flux evolution is represented in Fig. 5. Assuming a diffusion-controlled process, Fick's law governs the layer thickening rate: the oxygen flux is proportional to the gradient of oxygen concentration:

$$J_O(r_1) = -D_O \frac{\partial C_O}{\partial r} \quad (1)$$

and similarly for yttrium:

$$J_Y(r_2) = -D_Y \frac{\partial C_Y}{\partial r} \# \quad (2)$$

The two interfaces move according to Fig. 5, where r_1 decreases and r_2 increases.

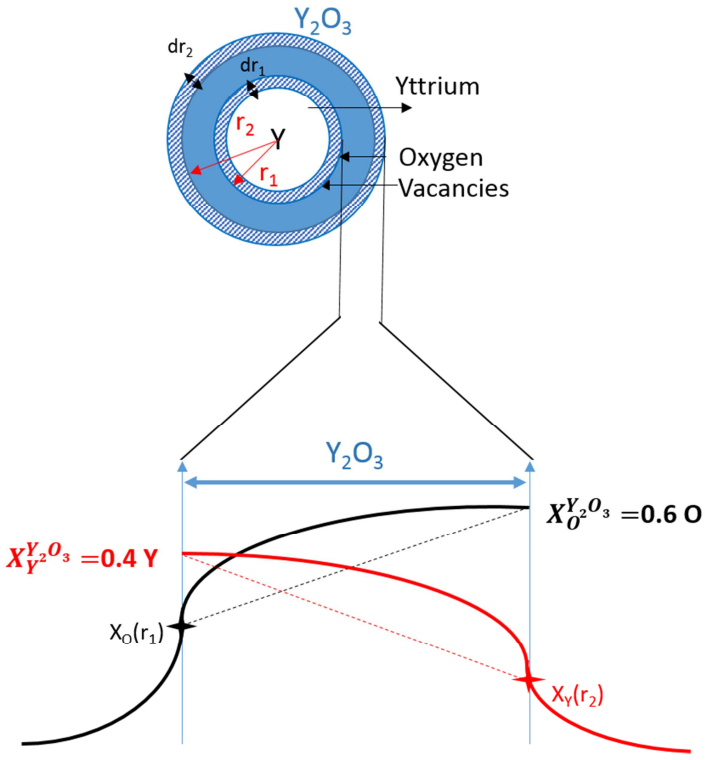

Figure 5: Evolution of the concentration in Y and O in the oxide layer, based on KE.

Assuming an affine gradient in the oxide layer between the two interfaces, the flux of oxygen and yttrium atoms can also be expressed as:

$$J_O = -\frac{1}{v_{at}} \frac{X_O^{Y_2O_3} - X_O(r_1)}{r_2 - r_1} D_O^{Y_2O_3} \quad (3)$$

$$J_Y = -\frac{1}{v_{at}} \frac{X_Y^{Y_2O_3} - X_Y(r_1)}{r_2 - r_1} D_Y^{Y_2O_3} \quad (4)$$

with $X_O^{Y_2O_3}$ =0.6 and $X_Y^{Y_2O_3}$ =0.4

The variation of r_1 and r_2 is expressed from a mass balance, as follows:

$$\frac{dr_1}{dt} = \frac{J_O(r_1)}{X_O(r_1)} \quad (5)$$

$$\frac{dr_2}{dt} = \frac{J_Y(r_2)}{X_Y(r_2)} \tag{6}$$

The diffusion coefficients $D_Y^{Y_2O_3}$ and $D_O^{Y_2O_3}$ could not be found in the literature; the initial value of r_1 was set to 10^{-9} m. The purpose of this model is to adjust the two diffusion coefficients in order to obtain the final experimental values: r_2 equals to 120 nm, and a (Fig. 6b)), the edge of the cavity equals to 60 nm. As it is shown in Fig. 6, to get the desired value of radii, the diffusion coefficients $D_Y^{Y_2O_3}$ and $D_O^{Y_2O_3}$ were arbitrarily set to 1.5×10^{-16} m²/s and 1.5×10^{-18}m²/s, respectively to fit the model.

Gaboriaud *et al.* established a diffusion coefficient for the yttrium self-diffusion in Y_2O_3, with large uncertainties [53], equal to:

$$D = 3.5 \times 10^{-9} m^2 s^{-1} \exp\left(-\frac{-72\ \frac{kcal}{mole}}{RT}\right) \tag{7}$$

This expression gives the same diffusion coefficient for yttrium, for a temperature equal to T=1450°C, which is consistent with the temperature reached during arc melting.

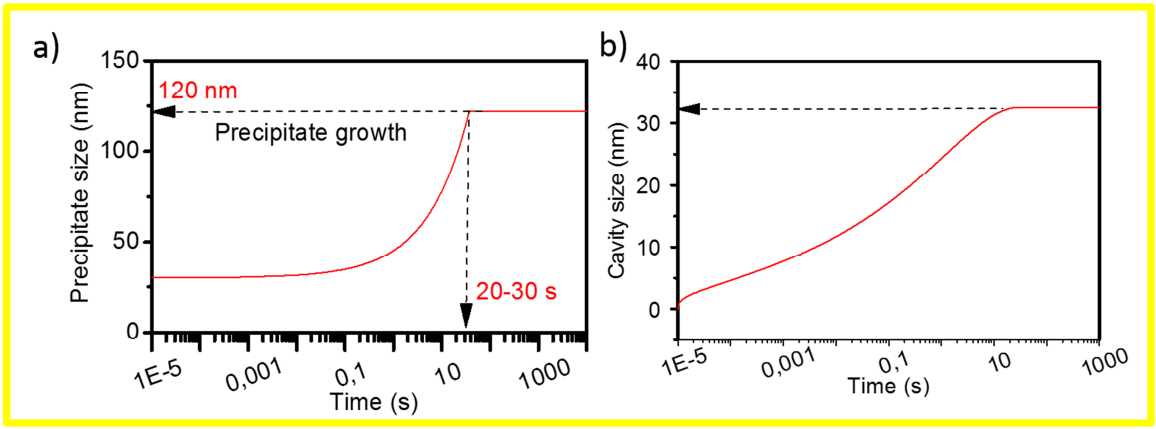

Figure 6: Evolution of a) the size of the precipitate b) the edge of the cavity, a.

Using this model, the time to form the precipitate and the cavity at this temperature is between 20 and 30 s, as shown in Fig 6, which is consistent with the melting process. This agreement supports the hypothesis of the formation of both precipitate and cavity in the liquid phase.

The KE has already been used for the processing of hollow nanostructures of Fe_2O_3, nanorods and nanospheres [41]. The morphology of the particles depends on the thermal treatment of diffusion. At high temperatures, the shape is spherical and at lower temperature the final shape is rectangular. Similarly, morphology differences were observed in the different precipitates, as shown in Fig. 7. The geometrical shape of the cavity varies from rectangular with facets to spherical (see Fig 7 a, b), while other morphologies are also observed (Fig. 7 c, d)).

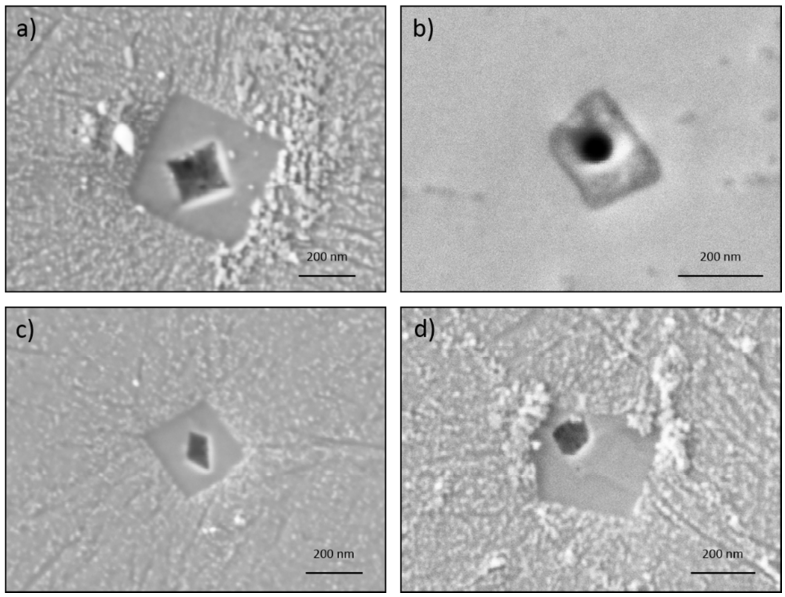

Figure 7: Low voltage Everhart-Thornley SE imaging of 4 hollow yttria precipitates. Several hollow morphologies are visible from round to square (white particles are colloidal silica particles used for polishing).

Overall, the KE could explain the formation of voids within the precipitates, as the prediction of the time needed to obtain the voids matches well the duration of the experimental procedure. The dark contrast observed in STEM-HAADF and the corresponding chemical maps reported in reference [33], and the Kirkendall effect-based diffusion model, support the conclusion that cavities are present within the precipitates.

5 Conclusion

The formation of Y_2O_3 precipitates, induced by the strong affinity between oxygen and yttrium, leads to the creation of micro and nano-crystallised areas in a Cu-based bulk metallic glass.

Two kinds of precipitates have been identified in the material: large ones with a cavity in their center, and full small ones. A strong size effect is evidenced to account for the presence of a void in the centre of an yttria precipitate. The cavity formation is explained by Kirkendall effect using vacancy diffusion mechanism, while the size and the shape of the yttria precipitate may be explained by the processing temperature.

Both types of precipitates seem to induce the crystallization of the BMG. However, small solid precipitates have been observed without any surrounding crystallized area. The size of the precipitate seems to have a significant effect on the size of the crystallized zones: micro-areas, created by the large hollow precipitates, and nano-areas, induced by small full precipitates. The latter have been highlighted using FIB tomography.

In this work, an original approach combining 2D and 3D structural investigations allowed to describe the structure caused by yttrium addition and understand the role of this microalloying in a Cu-based bulk metallic glass system on the mechanical properties. A tentative explanation for the precipitate formation was also proposed. Moreover, a model was created, and corroborated the experimental work, thus strengthening the hypothesis on the cavity formation by Kirkendall effect. This work leads to a significant step towards a better understanding of the influence of rare-earth elements minor additions on the microstructure and properties of BMGs. This work highlights the importance of controlling the precipitate fraction and crystallized areas to design novel metallic glasses with specifically optimized properties for target applications.

Acknowledgments

The microscopy work has been performed at the CLYM (Centre Lyonnais de Microscopie), a facility supported by the CNRS, the “GrandLyon” and the Rhône-Alpes Region. This work has been financially supported by the SIMAP Laboratory (GPM2). The authors thank Sebastien Gravier and Alexis Lenain for discussions and assistance regarding the samples processing. Maylise Nastar is gratefully acknowledged for fruitful and stimulating discussions.

Data Availability

The raw/processed data required to reproduce these findings cannot be shared at this time as the data also forms part of an ongoing study.

5 References

[1] M.M. Khan, A. Nemati, Z.U. Rahman, U.H. Shah, H. Asgar, W. Haider, Recent Advancements in Bulk Metallic Glasses and Their Applications: A Review, Crit. Rev. Solid State Mater. Sci. (2017) 1–36.

[2] C.H. Lin, C.H. Huang, J.F. Chuang, J.C. Huang, J.S.C. Jang, C.H. Chen, Rapid screening of potential metallic glasses for biomedical applications, Mater. Sci. Eng. C. 33 (2013) 4520–4526.

[3] A. Inoue, A. Takeuchi, Recent development and application products of bulk glassy alloys, Acta Mater. 59 (2011) 2243–2267.

[4] M. Mour, D. Das, T. Winkler, E. Hoenig, G. Mielke, M.M. Morlock, A.F. Schilling, Advances in porous biomaterials for dental and orthopaedic applications, Materials 3 (2010) 2947–2974.

[5] J.S.C. Jang, Y.S. Chang, T.H. Li, P.J. Hsieh, J.C. Huang, C.Y.A. Tsao, Plasticity enhancement of $Mg_{58}Cu_{28.5}Gd_{11}Ag_{2.5}$ based bulk metallic glass composites dispersion strengthened by Ti particles, J. Alloys Compd. 504 (2010) S102–S105.

[6] M. Meng, Z. Gao, L. Ren, H. Yang, S. Ma, Improved plasticity of bulk metallic glasses by electrodeposition, Mater. Sci. Eng. A. 615 (2014) 240–246.

[7] A. Inoue, W. Zhang, T. Zhang, K. Kurosaka, High-strength Cu-based bulk glassy alloys in Cu–Zr–Ti and Cu–Hf–Ti ternary systems, Acta Mater. 49 (2001) 2645–2652.

[8] H. Li, S. Pang, Y. Liu, L. Sun, P.K. Liaw, T. Zhang, Biodegradable Mg–Zn–Ca–Sr bulk metallic glasses with enhanced corrosion performance for biomedical applications, Mater. Des. 67 (2015) 9–19.

[9] T. Wang, Y.D. Wu, J.J. Si, Y.H. Cai, X.H. Chen, X.D. Hui, Novel Ti-based bulk metallic glasses with superior plastic yielding strength and corrosion resistance, Mater. Sci. Eng. A. 642 (2015) 297–303.

[10] J.J. Lewandowski, W.H. Wang, A.L. Greer, Intrinsic plasticity or brittleness of metallic glasses, Philos. Mag. Lett. 85 (2005) 77–87.

[11] M.A. El-Hadek, M. Kassem, Failure behavior of Cu–Ti–Zr-based bulk metallic glass alloys, J. Mater. Sci. 44 (2009) 1127–1136.

[12] S. Madge, Toughness of Bulk Metallic Glasses, Metals (Basel). 5 (2015) 1279–1305.

[13] X.H. Sun, Y. S. Wang, J. Fan et al., Plasticity improvement for dendrite/metallic glass matrix composites by pre-deformation, Mat. & Des. 86 (2015), 266-271.

[14] D. Liu, S. Lin, Z. Zhu, et al., The design and mechanical behaviors of in-situ formed ductile dendrite Ti-based bulk metallic glass composites with tailored composition and mechanisms, Mater. Sci. & Eng. A 732 (2018) 148-156.

[15] W. Guo, J. Saida, M. Zhao, et al., In-situ Ta-rich particle reinforced Zr-based bulk metallic glass matrix composites with tensile plasticity, J. Alloys Compd 775 (2019) 1002-1006.

[16] H. Huang, H. Ke, P. Zhang, et al., U-involved sphere-dispersed metallic glass matrix composites, Mat. & Des. 157 (2018) 371-376.

[17] S. Scudino, G. Liu, K.G. Prashanth, B. Bartusch, K.B. Surreddi, B.S. Murty, J. Eckert, Mechanical properties of Al-based metal matrix composites reinforced with Zr-based glassy particles produced by powder metallurgy, Acta Mater. 57 (2009) 2029–2039.

[18] J.S.C. Jang, J.B. Li, S.L. Lee, Y.S. Chang, S.R. Jian, J.C. Huang, T.G. Nieh, Prominent plasticity of Mg-based bulk metallic glass composites by ex-situ spherical Ti particles, Intermetallics. 30 (2012) 25–29.

[19] G. Q. Xie, D. Louzguine, M. Fukuhara, H. Kimura, A. Inoue, Cu particulate dispersed $Cu_{50}Zr_{50}Al_5$ bulk metallic glass composite with enhances electrical conductivity, Intermetallics. 18 (2010) 1973–1977.

[20] G. Xie, D. V. Louzguine-Luzgin, H. Kimura, A. Inoue, F. Wakai, Large-size ultrahigh strength Ni-based bulk metallic glassy matrix composites with enhanced ductility fabricated by spark plasma sintering, Appl. Phys. Lett. 92 (2008) 121907.

[21] R. Zheng, H.Yang, T. Liu, et al., Microstructure and mechanical properties of aluminum alloy matrix composites reinforced with Fe-based metallic glass particles, Mat. & Des. (2014), 512-518.

[22] S. Chen, L. Zhang, H.M. Fu, et al., Compressive mechanical properties and failure modes of Zr-based bulk metallic glass composites containing tungsten springs, Mat. & Des. 160 (2018) 652-660.

[23] W. Dmowski, Y. Yokoyama, A. Chuang, Y. Ren, M. Umemoto, K. Tsuchiya, A. Inoue, T. Egami, Structural rejuvenation in a bulk metallic glass induced by severe plastic deformation, Acta Mater. 58 (2010) 429-438.

[24] S. V Ketov, Y.H. Sun, S. Nachum, Z. Lu, A. Checchi, A.R. Beraldin, H.Y. Bai, W.H. Wang, D. V Louzguine-Luzgin, M.A. Carpenter, A.L. Greer, Rejuvenation of metallic glasses by non-affine thermal strain, Nature 524 (2015) 200-203.

[25] J. Lübke, A.G. Wilde, Cryogenic Rejuvenation of Metallic Glasses, Institut für Materialphysik, Westfälische Wilhems Universität Munster, (2014).

[26] N. Chen, L. Martin, D. V. Luzguine-Luzgin, A. Inoue, Role of Alloying Additions in Glass Formation and Properties of Bulk Metallic Glasses, Materials 3 (2010) 5320–5339.

[27] W.H. Wang, Roles of minor additions in formation and properties of bulk metallic glasses, Prog. Mater. Sci. 52 (2007) 540–596.

[28] N. Chen, D. V Louzguine-Luzgin, G.Q. Xie, T. Wada, A. Inoue, Influence of minor Si addition on the glass-forming ability and mechanical properties of Pd40Ni40P20 alloy, Acta Mater. 57 (2009) 2775–2780.

[29] H. Zhai, H. Wang, F. Liu, Effects of Sn addition on mechanical properties of Ti-based bulk metallic glass composites, Mat. & Des. 10 (2016, 782-789)

[30] Z.P. Chen, J.E. Gao, Y. Wu, H.X. Li, H. Wang, Z.P. Lu, Role of rare-earth elements in glass formation of Al–Ca–Ni amorphous alloys, J. Alloys Compd. 513 (2012) 387–392.

[31] E. Willbold, X. Gu, D. Albert, K. Kalla, K. Bobe, M. Brauneis, C. Janning, J. Nellesen, W. Czayka, W. Tillmann, Y. Zheng, F. Witte, Effect of the addition of low rare earth elements (lanthanum, neodymium, cerium) on the biodegradation and biocompatibility of magnesium, Acta Biomater. 11 (2015) 554–562.

[32] L. Deng, B. Zhou, H. Yang, X. Jiang, B. Jiang, X. Zhang, Roles of minor rare-earth elements addition in formation and properties of Cu–Zr–Al bulk metallic glasses, J. Alloys Compd. 632 (2015) 429–434.

[33] O. Baulin, M. Bugnet, D. Fabregue, et al, Improvement of mechanical, thermal and corrosion properties of Ni- and Al-free Cu-Zr-Ti metallic glass with yttrium addition, Materialia 1, 2018, 249-257

[34] M. Yan, J. Shen, T. Zhang, J. Zou, Enhanced glass-forming ability of a Zr-based bulk metallic glass with yttrium doping, J. Non. Cryst. Solids. 352 (2006) 3109–3112.

[35] Y. Zhang, J. Chen, G.L. Chen, X.J. Liu, Influence of yttrium addition on the glass forming ability in Cu–Zr–Al alloys, Mater. Sci. Eng. A. 483–484 (2008) 235–238.

[36] Z.P. Lu, C.T. Liu, W.D. Porter, Role of yttrium in glass formation of Fe-based bulk metallic glasses, Appl. Phys. Lett. 83 (2003) 2581–2583.

[37] G. Hao, F. Ren, Y. Zhang, J. Lin, Role of yttrium in glass formation of Ti-based bulk metallic glasses, Rare Met. 28 (2009) 68–71.

[38] T. Zhang, K. Kurosaka, A. Inoue, Thermal and Mechanical Properties of Cu-Based Cu-Zr-Ti-Y Bulk Glassy Alloys, Mater. Trans. 42 (2001) 2042–2045.

[39] Y. Zhang, J. Chen, G.L. Chen, X.J. Liu, Glass formation mechanism of minor yttrium addition in CuZrAl alloys, Appl. Phys. Lett. 89 (2006) 131904.

[40] E. Kirkendall, L. Thomassen, C. Upthegrove, Rates of Diffusion of Copper and Zinc in Alpha Brass, AIME 967 (1938)

[41] J. Cho, J. Park, Y. Kang, Preparation of Hollow Fe2O3 Nanorods and Nanospheres by Nanoscale Kirkendall Diffusion, and Their Electrochemical Properties for Use in Lithium-Ion Batteries, Scientific Reports 6 (2016) 38933

[42] J. Cho, H.S. Ju, Y.C. Kang, Applying nanoscale Kirkendall diffusion for template-free, kilogram-scale production of SnO2 hollow nanospheres via spray drying system, Scientific Reports 6 (2016) 23915.

[43] N. Gazit, G. Richter, A. Sharma, et al, Engineering of hollow AlAu2 nanoparticles on sapphire by solid state dewetting and oxidation of Al, Mat. & Des. 165 (2019), 107557.

[44] C. Desgranges, F. Lequien, E. Aublant, M. Nastar, D. Monceau, Depletion and voids formation in the substrate during high temperature oxidation of Ni-Cr-alloys, Oxid. Met. 79, (2013), 93-105.

[45] J. Cazaux, Material contrast in SEM: Fermi energy and work function effects, Ultramicroscopy 110, (2010) 242-253

[46] J. Cazaux, From the physics of secondary electron emission to image contrasts in scanning electron microscopy, Journal of Electron Microscopy 61 (2012) 261-284

[47] M. Phaneuf, Applications of focused ion beam microscopy to materials science specimens, Micron 30, (1999) 277-288.

[48] J. Orloff, M. Utlaut, L. Swanson, Applications of focused ion beams. In High Resolution Focused Ion Beams: FIB and its Applications, Springer, Boston, MA, (2003) 205-290

[49] J. Schindelin, I. Arganda-Carreras, E. Frise, V. Kaynig, M. Longair, T. Pietzsch, S. Preibisch, C. Rueden, S. Saalfeld, B. Schmid, J.-Y. Tinevez, D.J. White, V. Hartenstein, K. Eliceiri, P. Tomancak, A. Cardona, Fiji: an open-source platform for biological-image analysis, Nat. Methods. 9 (2012) 676–682.

[50] A. Argon, Plastic deformation in metallic glasses, Acta Metall. Mater. 27, (1979) 47-58

[51] T. Hufnagel, C.Schuh, M. Falk, Deformation of metallic glasses: Recent developments in theory, simulations, and experiments, Acta Materialia 109, (2016), 375-393

[52] K.N. Tu, U. Gösele, Hollow nanostructures based on Kirkendall effect: Design and stability considerations, Applied Physics Letters 86, (2005) 093111

[53] R.J., Gaboriaud, Self-Diffusion of yttrium in monocrystalline yttrium oxide: Y_2O_3, Journal of Solid State Chemistry 35, (1980) 252-261

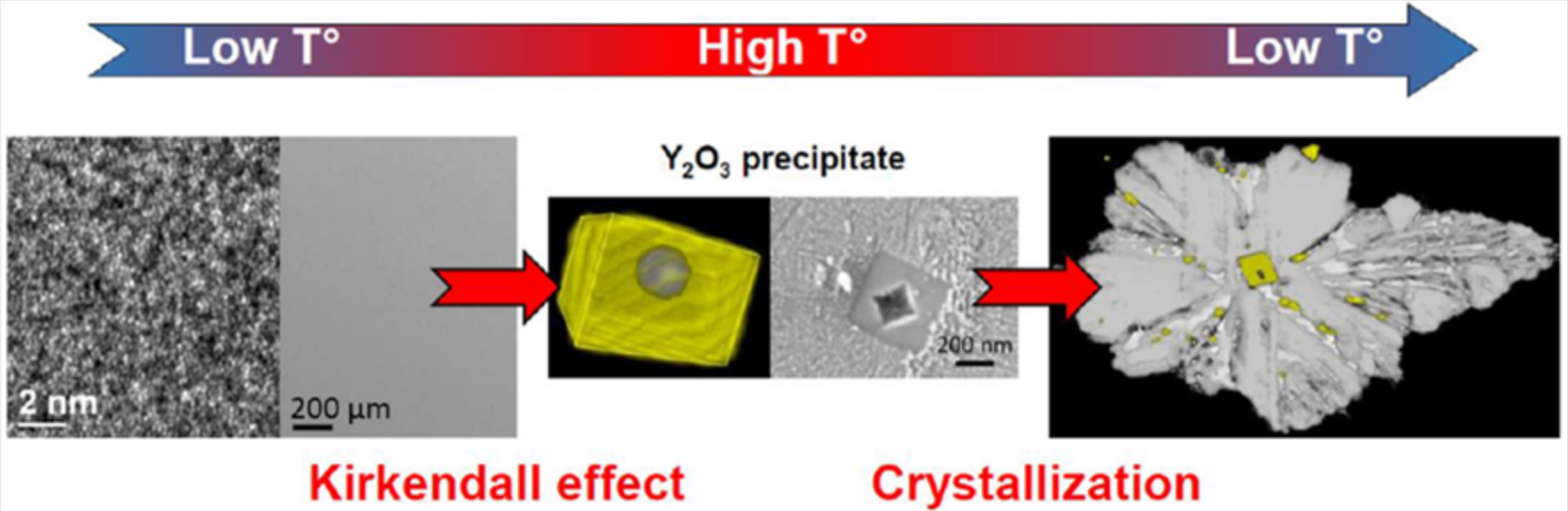
Low T°
High T°
Low T°
2 nm
200 µm
Y_2O_3 precipitate
200 nm
Kirkendall effect
Crystallization